Low Temperature Physics/Fizika Nizkikh Temperatur, 2017, v. 43, No. 5, pp. 683–691

Comparative Raman scattering study of $Ba_3MSb_2O_9$ (M=Zn, Co and Cu)

A. Glamazda[1,2], P. Lemmens[3],S.-H. Do[1], and K.-Y. Choi[1]

[1]*Department of Physics, Chung-Ang University, Seoul 156-756, Republic of Korea*
E-mail: kchoi@cau.ac.kr

[2]*B. Verkin Institute for Low Temperature Physics and Engeneering of the National Academy of Sciences of Ukraine 47 Nauky Ave, Kharkiv 61103, Ukraine*

[3]*Institute for Condensed Matter Physics, TU Braunschweig, Braunschweig D-38106, Germany*

Received October 11, 2016, published online March 24, 2017

Raman spectroscopy is combined with lattice dynamic calculations to investigate the magnetic and structural properties of the 6H-perovskite compounds $Ba_3MSb_2O_9$ (M = Zn, Co and Cu). Unlike the nonmagnetic $Ba_3ZnSb_2O_9$ compound, the magnetic counterparts $Ba_3MSb_2O_9$ (M = Co and Cu) show both lattice anomalies for temperatures below 100 K and develop highly correlated spin states below 50 K. This is ascribed to an instability of conventional magnetic excitations for the equilateral triangular antiferromagnet $Ba_3CoSb_2O_9$ and a coexistence of spin-orbital liquid and random singlet state for the decorated honeycomb compound $Ba_3CuSb_2O_9$ containing a nearly identical volume fraction of hexagonal and orthorhombic phases. Our results demonstrate that $Ba_3MSb_2O_9$ provides a rich reservoir for hosting diverse magnetic and structural phases as a function of the metal ion M.

PACS: **63.20.–e** Phonons in crystal lattices;
75.45.+j Macroscopic quantum phenomena in magnetic systems;
78.30.–j Infrared and Raman spectra.

Keywords: spin frustration, spin-phonon coupling, Raman scattering.

Introduction

Since the seminal work of Fazekas and Anderson, two-dimensional triangular antiferromagnets have become a focus of intense research due to the possibility of hosting quantum spin liquids [1]. Unlike conventional magnets, the magnetic moments in quantum spin liquids are long-range entangled and are in a coherent collective motion without breaking local symmetries. This novel state of matter entails topological order and fractionalization of spins, holding promise for a discovery of new quasiparticles as well as for potential applications of decoherence-free quantum computation. Prominent examples are κ-$(BEDT\text{-}TTF)_2Cu_2(CN)_3$ and $Et_nMe_{4-n}Sb[Pd(DMIT)_2]_2$ [2,3].

The 6H-perovskite family $Ba_3MA_2O_9$ (M = transition metals; A = Sb, Ti) realizes a stacked triangular lattice [4–9]. The basic building block of $Ba_3MA_2O_9$ consists of magnetic MO_6 and non-magnetic AO_6 octahedral layers. As the M^{2+} and A^{5+} ions occupy the crystallographically equivalent position, site and structural disorder is unavoidable, exerting a strong impact on their magnetic properties. Indeed, depending on the chemical variants, these compounds exhibit diverse ground states including quantum spin liquids, random singlet state, 120° ordering, and spin freezing. As such, it is essential to understand the relation between local structure and magnetism. Raman spectroscopy is an efficient and sensitive tool that can simultaneously probe lattice and spin excitations. The comparison of the Raman spectra between $Ba_3MA_2O_9$ (M = Zn, Co, and Cu) can thus shed a light on the interplay between lattice, orbital and spin degrees of freedom [10].

The nonmagnetic $Ba_3ZnSb_2O_9$ crystallizes in the $P6_3/mmc$ structure comprising the Sb_2O_9 bioctahedral slabs separated by the single ZnO_6 octahedral layer. For the case of $Ba_3CuSb_2O_9$, the face-sharing CuO_6 and SbO_6 octahedra form the $CuSbO_9$ bioctahedra stacked along the *c* axis. The $CuSbO_9$ dimers (so-called Cu–Sb dumbbells) are arranged between the alternating SbO_6 layers [4,5]. A decorated honeycomb lattice is derived from the original triangular lattice by virtue of electric-dipole interactions between Sb^{5+}–Cu^{2+} dumbbells. When the Cu/Sb stoichiometric ratio is larger

© A. Glamazda, P. Lemmens, S.-H. Do, and K.-Y. Choi, 2017

than 8%, the hexagonal phase is transformed into the orthorhombic phase below the collective Jahn–Teller transition at about 200 K [4]. The orthorhombic phase sample shows spin freezing below 110 mK or a random singlet state whose low-energy excitations are dictated by defect-induced spin textures. In the hexagonal Ba_3CuSbO_9 the Jahn–Teller distortion has a local, dynamic character, leading to the spin-orbital liquid state.

In $Ba_3CoSb_2O_9$, Co^{2+} ions have a Kramers doublet ground state due to spin-orbit coupling, resulting in an effective $S = 1/2$ equilateral triangular-lattice in the *ab* plane. $Ba_3CoSb_2O_9$ undergoes magnetic ordering at $T_N \sim 3.8$ K with the noncollinear 120° structure [7]. Inelastic neutron scattering results show the strong renormalization of the magnon dispersion, rotonlike minima, and line broadening throughout the entire Brillouin zone, which cannot be captured within a semiclassical theory.

In this paper, we report a comparative Raman scattering study of the three compounds $Ba_3MSb_2O_9$ (M = Zn, Cu, Co). We find lattice anomalies and a pronounced quasielastic response only for the magnetic compounds $Ba_3MSb_2O_9$ (M = = Cu and Co). This is discussed in terms of site and structural disorders as well as the formation of a highly correlated spin state.

Experimental details

Single crystals of $Ba_3MSb_2O_9$ (M = Cu, Co, Zn) were grown by the $BaCl_2$ flux method. For the synthesis of single crystals, polycrystalline samples of $Ba_3MSb_2O_9$ were first prepared using the recipes described in Ref. 11. The polycrystalline sample and $BaCl_2$ flux were mixed with 1:10 molar ratio and the mixtures were placed in a platinum crucible and heated in a muffle furnace. These mixtures were soaked at 1100, 1250, and 1200 °C for M = Cu, Co, and Zn compounds, respectively, during 5 hours and then were slowly cooled down to 900 °C at a rate of 2 °C/h. The obtained crystals were washed with water to remove the remaining fluxes. The crystals were crushed and ground for powder x-ray diffraction and energy dispersive x-ray spectroscopy (EDX), which confirmed a single phase of the $Ba_3MSb_2O_9$ crystals.

For the Raman scattering experiments, the samples were installed into a He-closed cycle cryostat with a temperature range $T = 7$–300 K. The incident light was focused into a 100-μm-diameter spot on the surface of the honeycomb (or triangular) *ab* plane. The scattered Raman spectra were recorded by using a triple spectrometer (Dilor-XY-500) equipped with a liquid-nitrogen-cooled CCD. The Raman spectra were measured in a quasi-backscattering geometry with the excitation line $\lambda = 532$ nm of a Nd:YAG (neodymium-doped yttrium aluminum garnet) solid-state laser. No discernible heating effects were observed. A Ne-lamp was used to calibrate the spectral position of the spectrometer.

Results and discussion

According to the recently published x-ray data, $Ba_3MSb_2O_9$ (M = Cu, Zn and Co) possesses $P6_3/mmc$ space group symmetry [12–14]. The total irreducible representation of Raman-active modes for the $P6_3/mmc$ group is given by $\Gamma = 5A_{1g}(aa, bb, cc) + 6E_{1g}(ac, bc) + 8E_{2g}(aa, bb,ab)$. In addition, there are the nine silent modes: $2A_{2g} + 6B_{1g} + B_{2g}$. In the orthorhombic phase of $Ba_3CuSb_2O_9$ (space group *Cmcm*), the factor group analysis predicts the irreducible representation: $\Gamma = 15A_g(aa, bb, cc)+11B_{1g}(ab)+8B_{2g}(ac) + +14B_{3g}(bc)$.

To assign the symmetries and eigenvectors of the observed phonon modes, we calculated the Γ-point phonon modes using shell-model lattice dynamical calculations implemented in the GULP package [15]. In the shell model treatment, the charge of the ion Z is given by a sum of a point core with charge X and a massless shell with charge Y, representing valence electrons. The ionic polarizability $\alpha = Y^2/K$ emanates from the interaction between the core and the shell, which is modeled by a harmonic oscillator with a force constant K. The interionic interactions are described by a combination of long-range Coulomb potentials and short-range Born–Mayer–Buckingham potentials between ions i and j:

$$V_{BM}(r) = A_{ij}\exp(-r/\rho_{ij}) - C_{ij}/r^6,$$

where A_{ij} and ρ_{ij} are the strength and the range of the repulsive interaction, respectively, and C_{ij} describes an attractive part with the interatomic distance r. Starting from well-documented data, the shell model parameters are optimized to reach a reasonable agreement with experimental Raman frequencies [16–19]. The resulting shell model parameters are listed in Table 1.

Table 1. List of shell model parameters for the shell-shell and core-shell interactions

Atom	A, eV	ρ, Å	C, eV·Å^6	X, |e|	Y, |e|	K, eV/ Å
Ba	4946.875	0.305541	0	2.0	0	0
Cu	3860.6	0.2427	0.0	1.0	1.0	99999
Zn	890.42	0.314	0	2.0	0	0
Co	1670.2416	0.2859	0	2.0	0	0
Sb	1480.529	0.3585	0	5.0	0	0
O	22764.0	0.149	27.88	0.869	–2.869	36

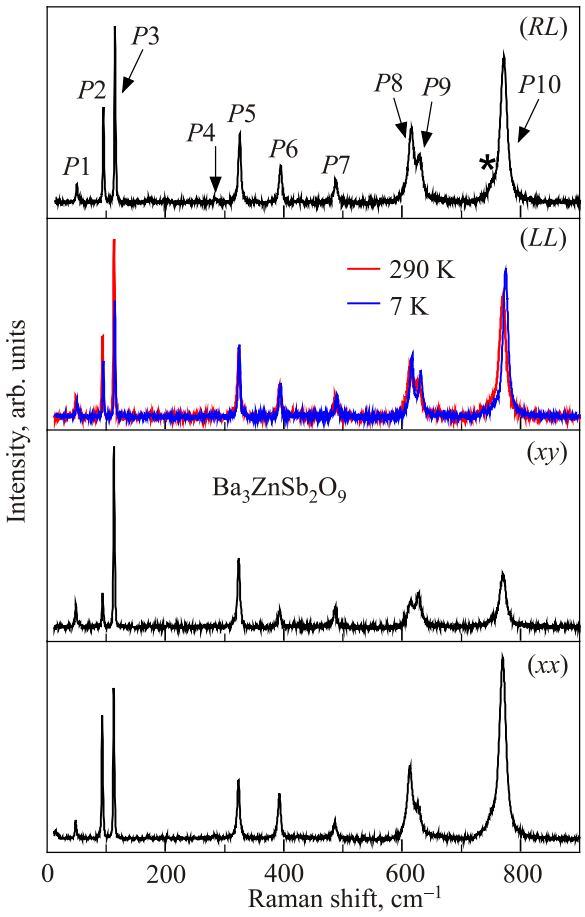

Fig. 1. (Color online) Raman spectra of $Ba_3ZnSb_2O_9$ measured in (*xx*), (*xy*), (*LL*) and (*RL*) polarizations.The peak at 754 cm^{-1} is marked with an asterisk.

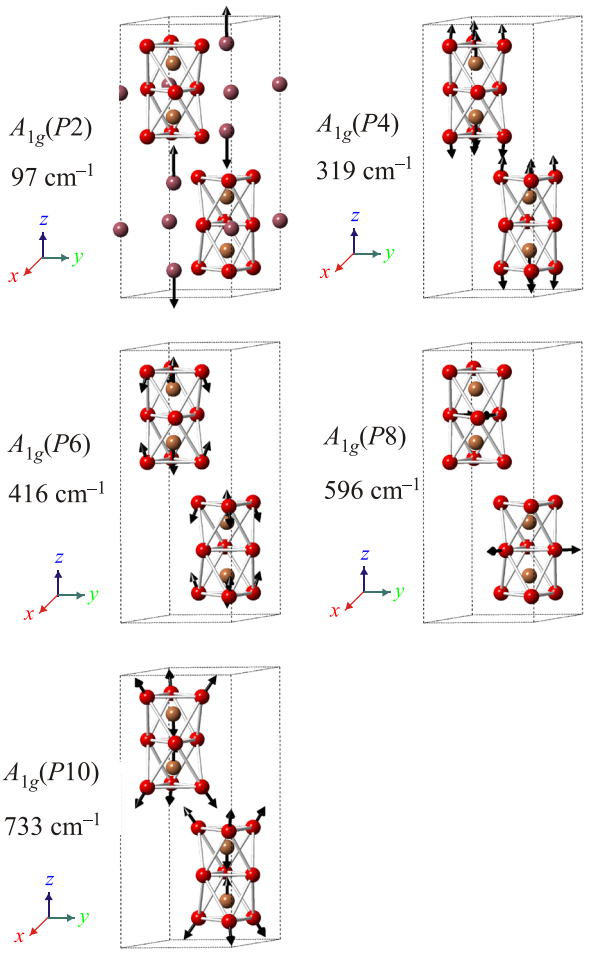

Fig. 2. (Color online) Schematic representation of calculated eigenvectors of the A_{1g} modes for $Ba_3ZnSb_2O_9$. The relative amplitude of the vibrations is represented by the arrow length. The red balls represent the oxygen ions, the mustard balls the Sb ions and the pink balls the Ba ions. The Ba ions are hidden for clarity whose vibrational amplitude is tiny. The symmetries and calculated frequencies are presented in the left side of figure.

In an attempt to clarify the structural and magnetic anomalies of $Ba_3CuSb_2O_9$ and $Ba_3CoSb_2O_9$, we first focus on the nonmagnetic counterpart $Ba_3ZnSb_2O_9$, which lacks a structural phase transition and disorder.

Figure 1 presents the Raman spectra of the $Ba_3ZnSb_2O_9$ single crystal measured at room temperature in four different (*xx*), (*xy*), (*LL*) and (*RL*) polarization configurations. Our spectra agree well with recently reported powder Raman spectra [5]. We observe 10 sharp, intense phonon modes which are described by Lorentzian profiles. Assigning the observed modes to the specific symmetry is made by considering the polarization-dependent Raman spectra and the shell-model calculation results as summarized in Table 2. The peaks at 49, 113, 325, 486 and 627 cm^{-1} which are largely insensitive to the polarization could be assigned to E_{2g} symmetry. The 93, 282, 393, 613 and 772 cm^{-1} modes are suppressed in the crossed polarization geometry and thus are assigned to A_{1g} symmetry. The calculated and experimental phonon energies agree well to each other. The representative displacement patterns for the A_{1g} modes are shown in Fig. 2. However, we find that the shoulder peak at 754 cm^{-1} the principal *P*10 mode could not be assigned to either E_{1g} or E_{2g}. Tentatively, we ascribe this peak to either the silent B_{1g} mode or two-phonon scattering. Noteworthy is that the linewidth of 754 cm^{-1} mode amounts to 23 cm^{-1} that is more than two times broader than the linewidth of the principal modes. As a rule, the silent mode can be induced by defects or local lattice distortions.

Figure 3(a) shows the temperature dependence of the Raman spectra taken in the (*LL*) polarization geometry. The circular polarization is chosen for the better coupling of incident photons to phonons in the hexagonal crystal basis. The phonon parameters of the 325.4 E_{2g} (*P*5) and 772 cm^{-1} A_{1g} (*P*10) modes are extracted from the fit to Lorentzian profiles. The results are summarized in Fig. 3(b). The temperature-dependent peak energy is described in terms of the anharmonic model [20]:

$$\omega(T) = \omega_0 + C\left[1 + 2/\left(e^x - 1\right)\right], \qquad (1)$$

Table 2. List of the observed modes, the phonon symmetries and the calculated frequencies in cm^{-1} at the Γ-point

	$Ba_3ZnSb_2O_9$			
	Exp., cm^{-1}	Calc., cm^{-1}	Symmetry	Description
*P*1	49	40	E_{2g}	Ba(1) and Ba(2) out-of-phase vibrations in the *xy* plane and stretching vibrations of Sb_2O_9
*P*2	93	97	A_{1g}	Ba(2) out-of-phase stretching vibrations along the *z* axis
*P*3	113	123	E_{2g}	Ba(1) and Ba(2) out-of-phase stretching vibrations in *xy* plane
*P*4	282	319	A_{1g}	O(2) and Sb out-of-phase stretching vibrations
*P*5	325	339	E_{2g}	O(1) and O(2) stretching vibrations
*P*6	393	416	A_{1g}	O(2) out-of-phase stretching vibrations
*P*7	486	491	E_{2g}	Sb_2O_9 stretching vibrations in the *xy* plane
*P*8	613	596	A_{1g}	O(1) breathing vibrations in *xy* plane
*P*9	627	665	E_{2g}	Sb_2O_9 stretching vibrations
*P*10	772	733	A_{1g}	O(2) and Sb out-of-phase stretching vibrations

where ω_0 is the harmonic frequency of the optical mode, $x = \hbar\omega_0/(2k_BT)$, and C is constant. In a similar manner, the full width at half maximum (FWHM) is described by

$$\Gamma(T) = \Gamma_0 + A\left[1 + 2/\left(e^x - 1\right)\right], \qquad (2)$$

where Γ_0 is the FWHM at $T = 0$ and A is constant. As evident from Fig. 3 (b), the lattice anharmonicity provides a reasonable description of the temperature dependence of the phonon frequencies and FWHM (see the dashed lines in Fig. 3 (b)). We can find no indications for lattice instabilities and imperfections. Consequently, the phonon spectra of $Ba_3ZnSb_2O_9$ can serve as a reference for studying the more complex magnetic counterparts $Ba_3CuSb_2O_9$ and $Ba_3CoSb_2O_9$.

Now we turn to the uniform triangular antiferromagnet $Ba_3CoSb_2O_9$. Figure 4(a) exhibits the Raman spectra of $Ba_3CoSb_2O_9$ taken in (*xx*), (*xy*), (*LL*) and (*RL*) polarization

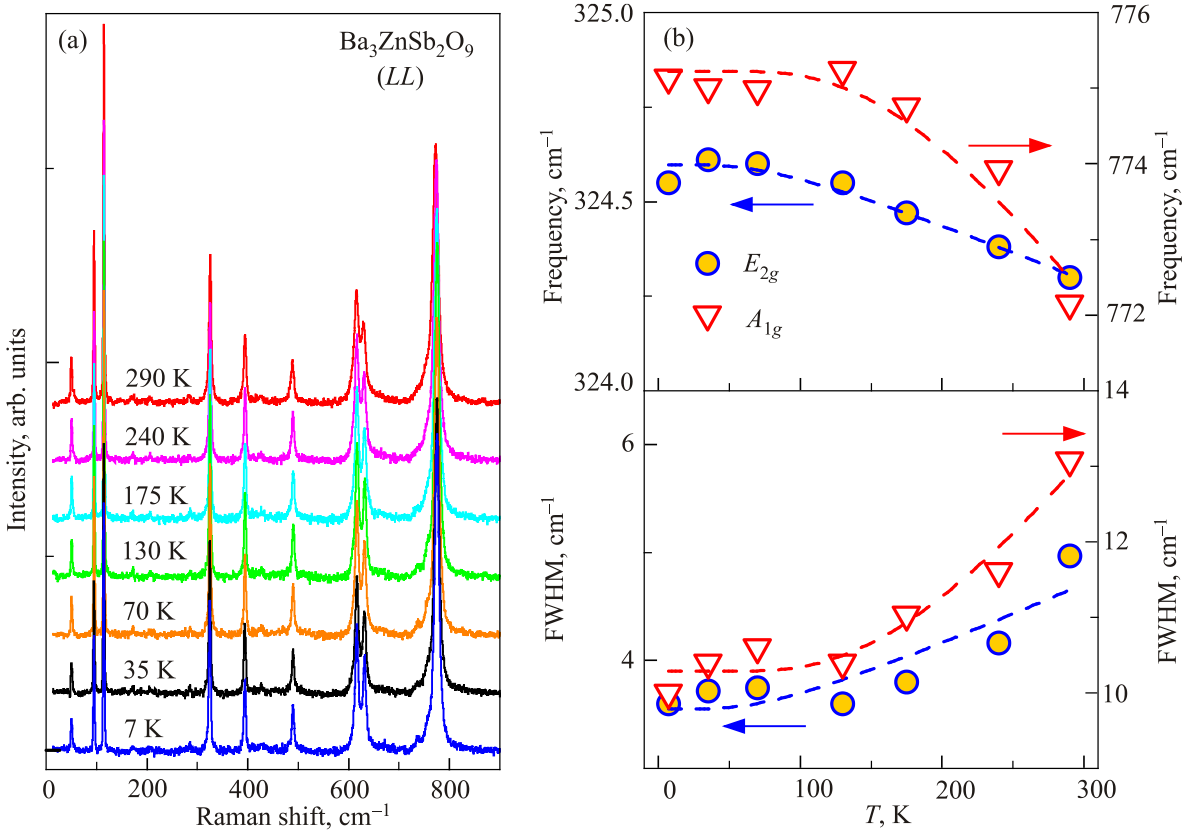

Fig. 3. (Color online) (a) Temperature dependence of Raman spectra of $Ba_3ZnSb_2O_9$ measured in (*LL*) polarization. (b) Temperature-dependent frequency and linewidth of the 325.4 (*P*5) and 772 cm^{-1} (*P*10) mode. The dashed lines are fits to Eqs. (1) and (2).

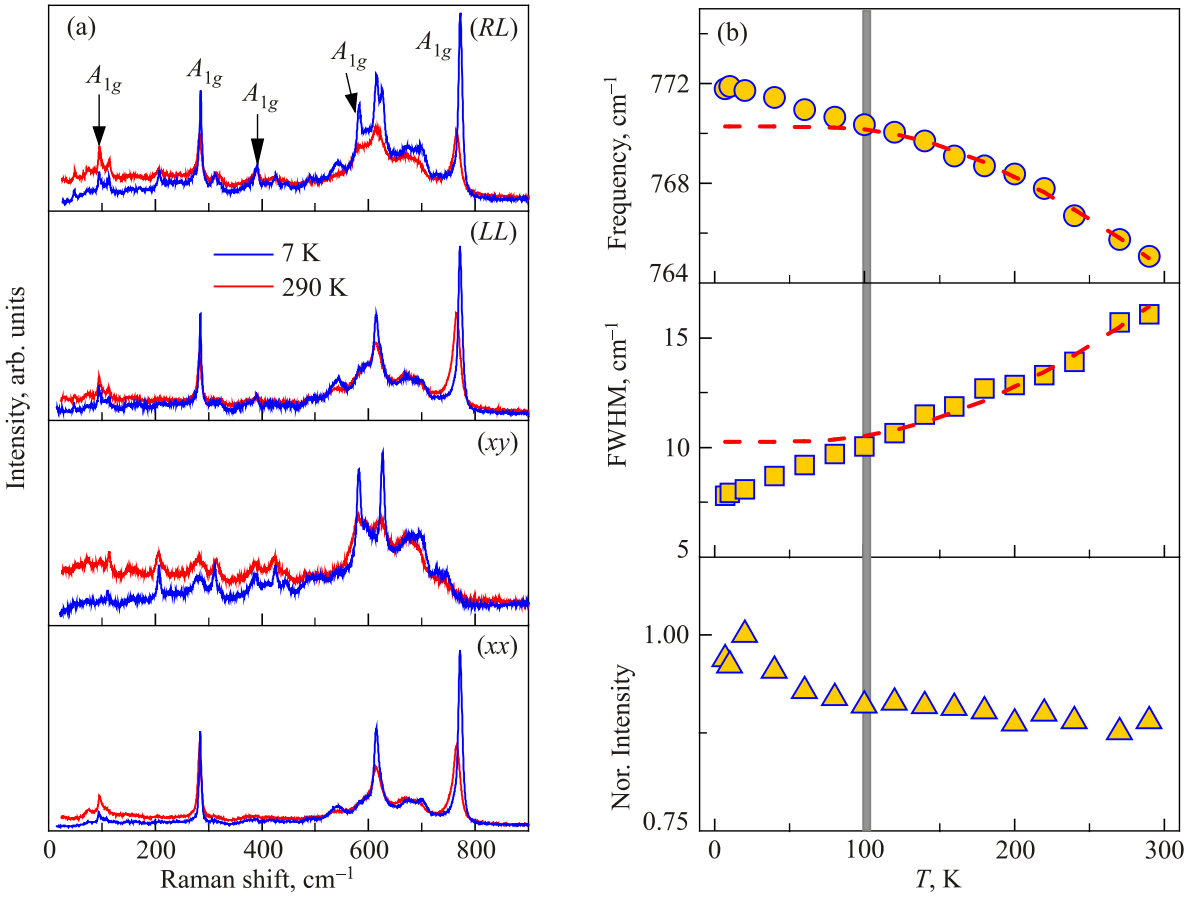

Fig. 4. (Color online) (a) Comparison of Raman spectra of $Ba_3CoSb_2O_9$ at $T = 7$ and 290 K taken in (*xx*), (*xy*), (*LL*) and (*RL*) polarizations. (b) Temperature dependence of the frequencies, full widths at half maximum, and normalized integrated intensities of the 762 cm^{-1} mode. The phonon intensity is corrected for the Bose thermal factor. The red dashed lines are fits to Eqs. (1) and (2). The vertical bar indicates the onset of short-range spin correlations.

configurations at $T = 7$ and 290 K. We identify a one-to-one correspondence of the A_{1g} vibrational modes between $Ba_3ZnSb_2O_9$ and $Ba_3CoSb_2O_9$: 93→95, 282→283, 393→390, 613→614, 772→765 cm^{-1}. The phonons of $Ba_3CoSb_2O_9$ are approximately two times broader than those of $Ba_3ZnSb_2O_9$. In addition, there are a number of the poorly resolved broad bands which may be ascribed to the doubly degenerate vibrations or multiphonon scatterings. These features suggest that $Ba_3CoSb_2O_9$ contains site disorders. In Fig. 4(b) we plot the temperature dependence of the

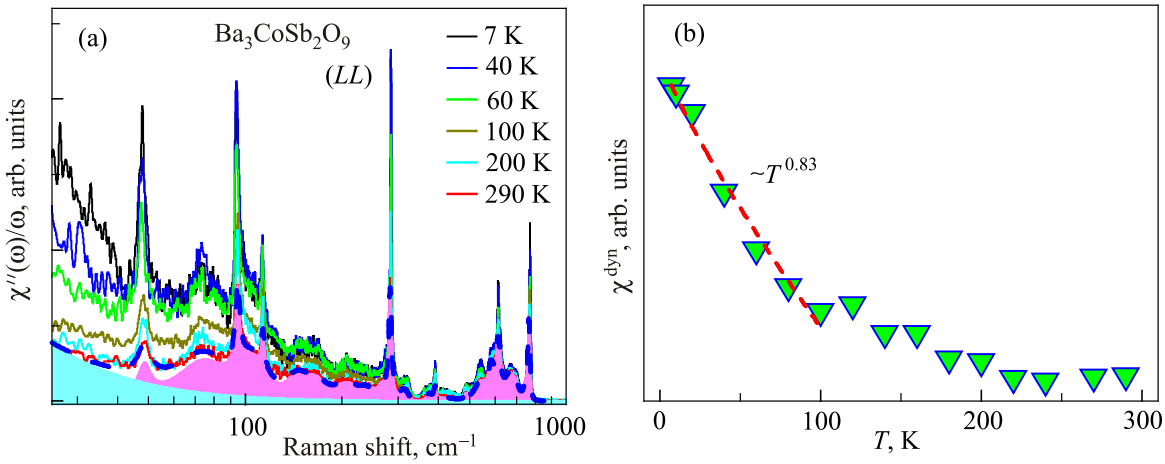

Fig. 5. (Color online) (a) Raman conductivity $\chi''(\omega)/\omega$ of $Ba_3CoSb_2O_9$ at various temperatures. The cyan shading is a magnetic continuum and the magenta shading represents the contribution due to phonons and multiphonons. (b) Temperature dependence of the dynamic Raman susceptibility deduced from the Kramers–Kronig relation. The dashed line is a power-law fit to the data, $\chi^{dyn}n(T) \sim T^{\alpha}$.

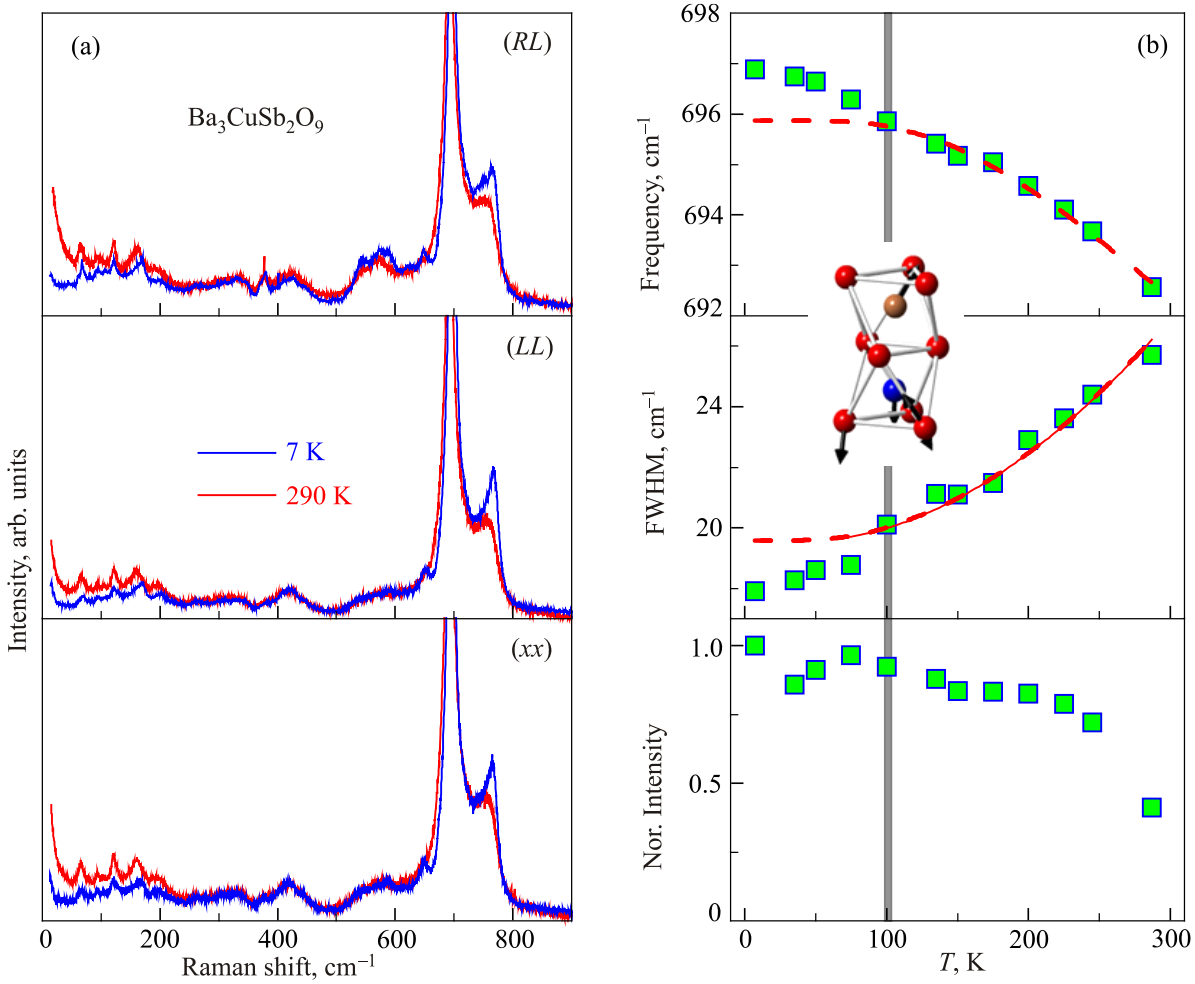

Fig. 6. (Color online) (a) Comparison of Raman spectra of $Ba_3CuSb_2O_9$ at T = 7 and 290 K in (xx), (LL) and (RL) polarization. (b) Temperature dependence of the frequencies, full widths at half maximum, and normalized integrated intensities of the 697 cm^{-1} mode. The phonon intensity is corrected for the Bose thermal factor. The inset depicts the eigenvectors of the 697 cm^{-1} mode. The relative amplitude of the vibrations is given by the arrows. The blue/mustard balls stand for the Cu/Sb ions and the red ones for the oxygen ions. The red dashed lines are fits to Eqs. (1) and (2).

772 cm^{-1} mode. Both the peak frequency and the linewidth deviate from the anharmonic model for temperatures below T = 100 K. Possibly, this is due to spin-lattice coupling.

The inelastic neutron scattering data give a hint to a partial fractionalization of spin excitations [9]. Raman scattering can also probe the low-energy magnetic excitations through double spin-flip processes. Indeed, we observe a systematic evolution of the background scattering with temperature. As the low-energy excitations are mainly affected, defect-induced excitations are unlikely as their origin. We calculate the dynamic Raman susceptibility to detail the dynamical properties of collective excitation possibly pertaining to the S = 1/2 XXZ triangular antiferromagnet. The Raman response $\chi''(\omega)$ is first obtained from the raw Raman spectra S(ω) using the relation $S(\omega) = \chi''(\omega)/(1-\exp(-\hbar\omega/k_BT))$ and thereby the Raman conductivity $\chi''(\omega)/\omega$ is derived. As shown in Fig. 5 (a), $\chi''(\omega)/\omega$ in (LL) polarization displays a quasielastic response (marked by a cyan shading), which increases gradually with decreasing temperature. Using the Kramers–Kronig relation the dynamic Raman susceptibility is defined as follows [21]:

$$\chi^{dyn} = \lim_{\omega\to 0}\chi(k=0,\omega) \equiv \frac{2}{\pi}\int_0^\infty \frac{\chi''(\omega)}{\omega}d\omega\,. \qquad (3).$$

Here, the integration of $\chi''(\omega)/\omega$ was made over the energy range of 25–350 cm^{-1} and the obtained $\chi^{dyn}(T)$ is presented in Fig. 5(b). The continuous increase of $\chi^{dyn}(T)$ with decreasing temperature resembles the temperature dependence of the static susceptibility. A close look unveils that $\chi^{dyn}(T)$ exhibits a power-law increase $T^{0.83}$ upon cooling down through T = 100 K. Around this temperature, the phonon dynamics deviates from the anharmonic model. Thus, we conclude that this temperature gives an energy scale for the onset of short-range correlations in the triangular plane. The less pronounced temperature dependence of $\chi^{dyn}(T)$ at high temperatures, accompanying a slope

change, is ascribed to a crossover to a pure paramagnetic phase with uncorrelated spins [22].

Next, we discuss the results of the $Ba_3CuSb_2O_9$ compound. Figure 6(a) presents the Raman spectra measured in three different polarizations at $T = 7$ and 290 K. The Raman spectra of $Ba_3CuSb_2O_9$ are unlike those of $Ba_3ZnSb_2O_9$ and $Ba_3CoSb_2O_9$. This means that the Cu compound has a different crystal structure from the Zn and Co compounds. It is known that the Cu/Sb off-stoichiometry brings about a hexagonal-to-orthorhombic Jahn–Teller (JT) transition at about $T_S = 200$ K [4]. Even the samples in the same batch contain a different amount of off-stoichiometry. The studied crystal comprises two structurally distinct environments: the static JT distorted orthorhombic phase and the dynamic spin-orbital entangled hexagonal phase. Due to the Cu^{2+}/Sb^{5+} site disorders within the $CuSbO_9$ bioctahedra and the microscopic coexistence of the hexagonal and orthorhombic phases the phonon modes form the broad bands [5]. Noticeably, the two pronounced modes at 697 and 765 cm^{-1} are clearly resolved. Figure 6(b) shows the temperature dependence of the 697 cm^{-1} mode corresponding to the stretching vibrations of $CuSbO_9$. It is evident that the temperature dependence of both the peak frequency and the linewidth is not described within the anharmonic model below $T = 100$ K.

A recent Raman study of the hexagonal and orthorhombic samples of $Ba_3CuSb_2O_9$ revealed that the 500–600 cm^{-1} oxygen stretching vibrations provide a good measure of discriminating the two phases [5,14]. The local symmetry breaking induced by the JT distortion leads to the splitting in the face-shared oxygen modes at around 550 cm^{-1} and the appearance of the additional peak in the orthorhombic phase. This motivates us to scrutinize the Raman spectra of $Ba_3CuSb_2O_9$ in the frequency range of 500–700 cm^{-1} as zoomed in Fig. 7(a). The peaks at 540 and 590.8 cm^{-1} marked with shaded Lorentzian curves correspond to the hexagonal and orthorhombic phase, respectively. From the relative ratio of their integrated intensity, the volume fraction of the hexagonal and orthorhombic phase is estimated to be about 40 and 60%, respectively.

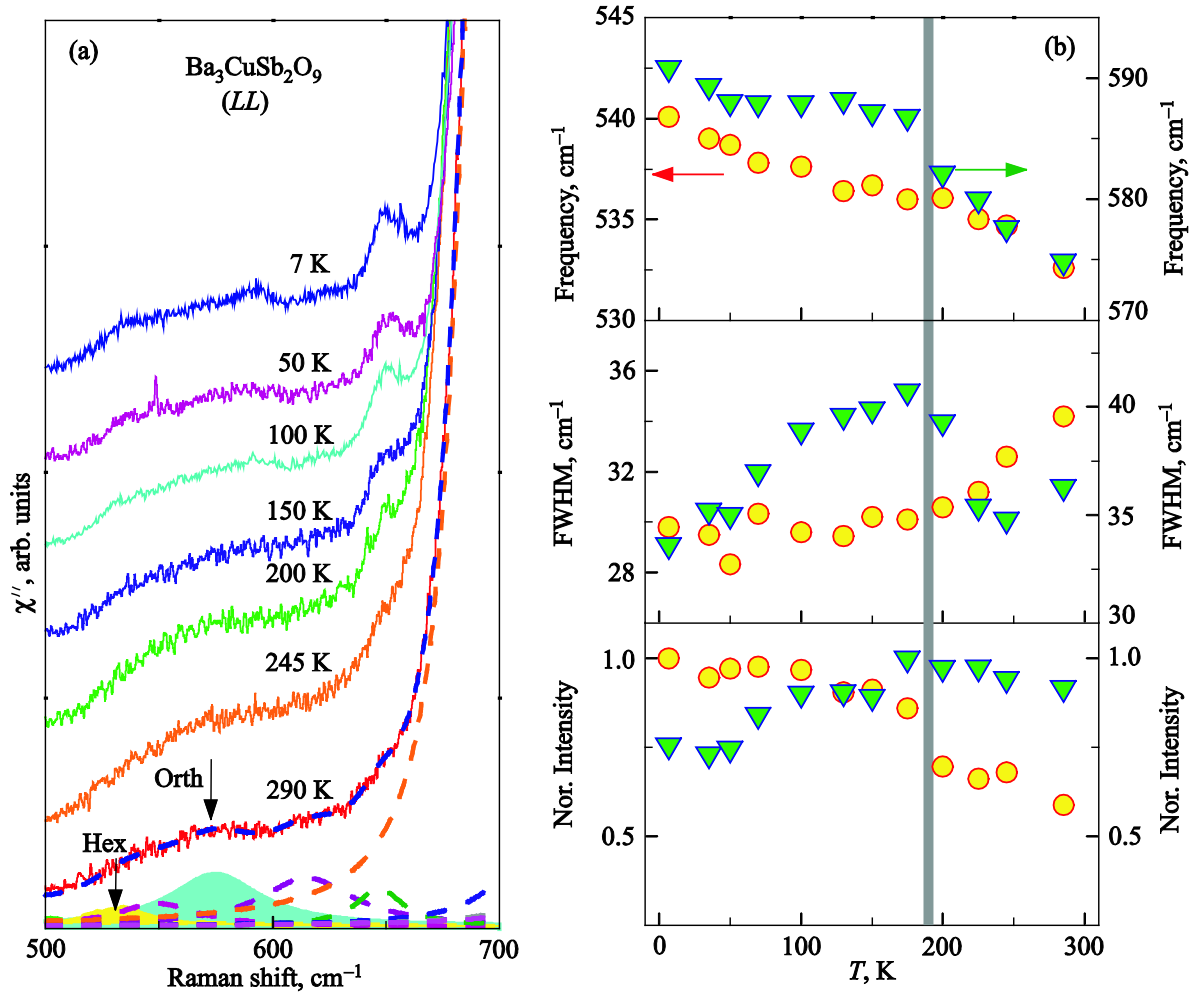

Fig. 7. (Color online) (a) The Bose corrected Raman spectra of $Ba_3CuSb_2O_9$ in (*LL*) polarization. The spectra are vertically shifted for clarity. The yellow and green shadings are ascribed to the hexagonal and orthorhombic phases, respectively. (b) Temperature dependence of the frequencies, linewidths, and normalized integrated intensities of the hexagonal (540 cm^{-1}) and orthorhombic (590.8 cm^{-1}) related phase. The vertical bar indicates the static Jahn–Teller transition temperature.

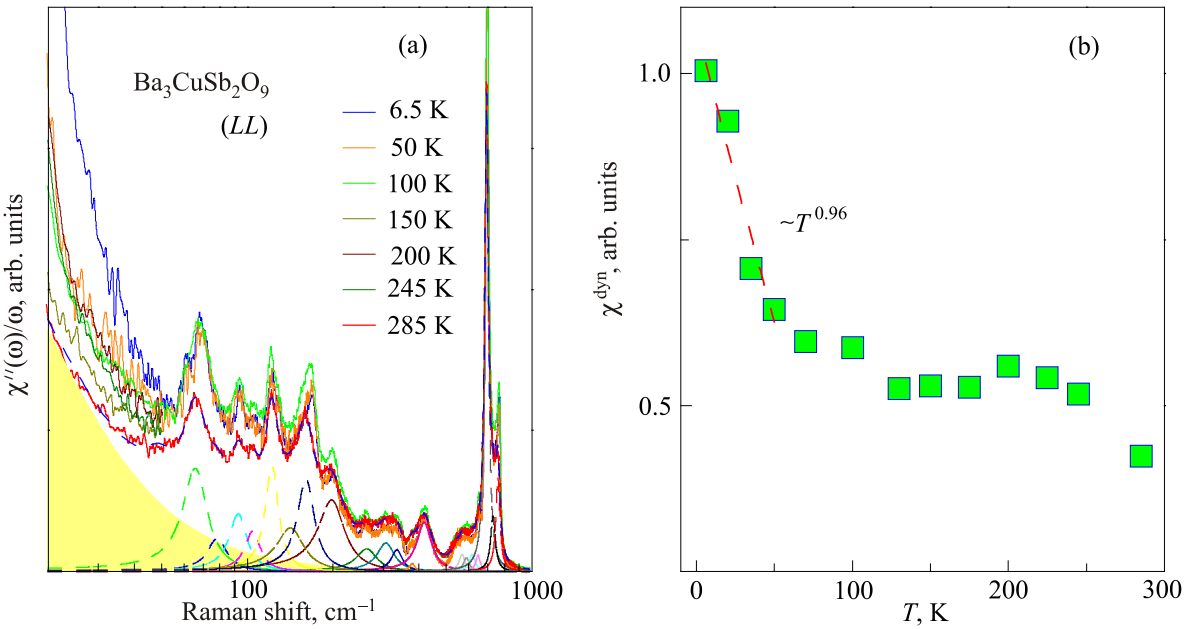

Fig. 8. (Color online) Raman conductivity χ''/ω of $Ba_3CuSb_2O_9$ taken in (*LL*)-polarization at various temperatures. The yellow shading indicates the magnetic scattering. (b) Temperature dependence of the dynamic Raman susceptibility obtained by the integration of χ''/ω over the frequency range of 17–450 cm^{-1}.

From fitting the 540 and 590.8 cm^{-1} modes to a sum of Lorentzian profiles, we extract the temperature dependence of the frequencies, linewidths, and intensities as summarized in Fig. 7(b). The errors are less than a symbol size. Only the orthorhombic-phase related 590.8 cm^{-1} mode exhibits a distinct anomaly at about 200 K, confirming a transition to the static JT distortion [5]. These results demonstrate that spin dynamics of $Ba_3CuSb_2O_9$ is dominated by a combined effect of a spin-orbital liquid and a random singlet state.

Finally, we analyze the Raman conductivity of $Ba_3CuSb_2O_9$, focusing on low-energy excitations. As displayed in Fig. 8 (a), χ''/ω shows a pronounced peak at about $\omega = 0$, which becomes stronger with decreasing temperature. The quasielastic response (marked by shading) was integrated over the frequency interval of 17–450 cm^{-1} and the resulting dynamic Raman susceptibility $\chi^{dyn}(T)$ is plotted in Fig. 8 (b) as a function of temperature. Similarly to $Ba_3CoSb_2O_9$, $\chi^{dyn}(T)$ of $Ba_3CuSb_2O_9$ displays a steep increase with the asymptotic power-law behavior of $T^{0.96}$. The weaker temperature dependence of $\chi^{dyn}(T)$ above 50 K suggests a crossover from strongly correlated spins to weakly interacting spin state. This suggests that $Ba_3CoSb_2O_9$ and $Ba_3CuSb_2O_9$ have the similar magnetic energy scale.

Conclusion

In summary, we have presented a comparative Raman scattering study of the 6H-perovskite compounds $Ba_3MSb_2O_9$ (M = Zn, Co and Cu). We observe no anomalous lattice dynamics for the nonmagnetic Zn sample. In contrast, both the uniform triangular antiferromagnet $Ba_3CoSb_2O_9$ and the honeycomb lattice $Ba_3CuSb_2O_9$ show (i) much broader phonon peaks than $Ba_3ZnSb_2O_9$ due to site disorders, (ii) the deviations from an anharmonic model below 100 K, and (iii) the development of a highly correlated spin state below 50 K. In addition, an analysis of the oxygen stretching vibrations of $Ba_3CuSb_2O_9$ unveils the coexistence of hexagonal and orthorhombic phases with nearly identical volume fraction. Our results demonstrate that $Ba_3MSb_2O_9$ hosts a rich variety of magnetic and structural phases emergent from the original stacked triangular lattice with $P6_3/mmc$ structure.

Acknowledgment

This work was supported by the Korea Research Foundation (KRF) grant funded by the Korea government (MEST) (Grant No. 2009-0093817 and No. 2016-911392), as well as by German-Israeli Foundation (GIF, 1171-486 189.14/2011), the NTH-School Contacts in Nanosystems:Interactions, Control and Quantum Dynamics, the Braunschweig International Graduate School of Metrology and DFG-RTG 1952/1, Metrology for Complex Nanosystems. S.H.D. was supported by Chung-Ang University Research Assistant Fellowship.

1. P. Fazekas and P.W. Anderson, *Philos. Mag.* **30**, 423 (1974).
2. Y. Shimizu, K. Miyagawa, K. Kanoda, M. Maesato, and G. Saito, *Phys. Rev. Lett.* **91**, 107001 (2003).
3. M. Yamashita, N. Nakata, Y. Senshu, M. Nagata, H.M. Yamamoto, R. Kato, T. Shibauchi, and Y. Matsuda, *Science* **328**, 1246 (2010).
4. S. Nakatsuji, K. Kuga, K. Kimura, R. Satake, N. Katayama, E. Nishibori, H. Sawa, R. Ishii, M. Hagiwara, F. Bridges, T.U.

Ito, W. Higemoto, Y. Karaki, M. Halim, A.A. Nugroho, J.A. Rodriguez-Rivera, M.A. Green, and C. Broholm, *Science* **336**, 559 (2012).
5. N. Drichko, C. Broholm, K. Kimura, R. Ishii, and S. Nakasutji, *Phys. Rev. B* **93**, 184425 (2016).
6. Y. Wakabayashi, D. Nakajima, Y. Ishiguro, K. Kimura, T. Kimura, S. Tsutsui, A.Q.R. Baron, K. Hayashi, N. Happo, S. Hosokawa, K. Ohwada, and S. Nakatsuji, *Phys. Rev. B* **93**, 245117 (2016).
7. Y. Doi, Y. Hinatsu, and K. Ohoyama, *J. Phys.: Condens. Matter* **16**, 8923 (2004).
8. H.D. Zhou, C. Xu, A.M. Hallas, H.J. Silverstein, C.R. Wiebe, I. Umegaki, J.Q. Yan, T.P. Murphy, J.-H. Park, Y. Qiu, J.R.D. Copley, J.S. Gardner, and Y. Takano, *Phys. Rev. Lett.* **109**, 267206 (2012).
9. J. Ma, Y. Kamiya, T. Hong, H. B. Cao, G. Ehlers, W. Tian, C. D. Batista, Z. L. Dun, H. D. Zhou, and M. Matsuda, *Phys. Rev. Lett.* **116**, 087201 (2016).
10. K.-Y. Choi, P. Lemmens, P. Scheib, V. Gnezdilov, Yu.G. Pashkevich, J. Hemberger, A. Loidl, and V. Tsurkan, *J. Phys.: Condens. Matter* **19**, 145260 (2007).
11. H.D. Zhou, E.S. Choi, G. Li, L. Balicas, C.R. Wiebe, Y. Qiu, J.R.D. Copley, and J.S. Gardner, *Phys. Rev. Lett*. **106**, 147204 (2011).
12. M.W. Lufaso, E. Hopkins, S.M. Bell, and A. Llobet, *Chem. Mater.* **17**, 4250 (2005).
13. K. Naruse, T. Kawamata, M. Ohno, Y. Matsuoka, H. Sudo, H. Nagasawa, Y. Hagiya, T. Sasaki, and Y. Koike, *J. Phys.: Conf. Ser.* **568**, 042014 (2014).
14. N. Katayama, K. Kimura, Y. Han, J. Nasu, N. Drichko, Y. Nakanishi, M. Halim, Y. Ishiguro, R. Satake, E. Nishibori, M. Yoshizawa, T. Nakano, Y. Nozue, Y. Wakabayashi, S. Ishihara, M. Hagiwara, H. Sawa, and S. Nakatsuji, *Proc. Natl. Acad. Sci. USA* **112**, 9305 (2015).
15. G.D. Gale, *J. Chem. Soc., Faraday Trans*. **93**, 629 (1997).
16. C.A.J. Fisher, V.M.H. Prieto, and M.S. Islam, *Chem. Mater.* **20**, 5907 (2008).
17. M.C. Castro Jr, E.F.V. Carvalho, W. Paraguassu, A.P. Ayala, F.C. Snyder, M.W. Lufaso, and C.W. de A. Paschoal, *J. Raman Spectroscopy* **40**, 1205 (2009).
18. R. Pandey, J.D. Gale, S.K. Sampath, and J.M. Recio, *J. Am. Ceram. Soc*. **82**, 3337 (1999).
19. M.S. Islam and L.J. Winch, *Phys. Rev. B* **52**, 10510 (1995).
20. M. Balkanski, R.F. Wallis, and E. Haro, *Phys. Rev. B* **28**, 1928 (1983)
21. *Frontiers in Solid State Sciences: Selected Topics in Magnetism* L.C. Gupta and M. S. Multani (eds.), World Scientific, Singapore (1993), Vol. 2.
22. A. Glamazda, P. Lemmens, S.-H. Do, Y.S. Choi, and K.-Y. Choi, *Nat. Commun*. **7**, 12286 (2016).